Supporting Information

Construction of N, P doped 3D dendritic-free lithium metal anode by using silicon-containing lithium metal

Yuanxing Zhang [a], Borong Wu*[ab], Daobin Mu*[a], Chengwei Ma[a], Xinyu Zhang [a], Yuanshen Wang[a], Zhiguang Zhao, Tao Liu and Chengcai Liu[a]

[a] *School of Materials Science and Engineering, Beijing Key Laboratory of Environment Science and Engineering, Beijing Higher Institution Engineering Research Center of Power Battery and Chemical Energy Materials, Beijing Institute of Technology, Beijing, 100081, PR China.*

[b] *Beijing Institute of Technology, Chongqing Innovation Center, Chongqing 401120, China*

E-mail: wubr@bit.edu.cn, mudb@bit.edu.cn;

Experimental Section

***Doping modification of lithium metal (DLi/LiSi$_x$) synthesis**:* The DLi/LiSi$_x$ melt was prepared by heating the pure Li foil and Si_3N_4 powder in stainless steel crucible in an Ar-filled glovebox at 450 ºC for 10 hours. The Lithium-Silicon alloy melt was prepared by adding 40mg Si_3N_4 powder into the 2 g Li melt under continuously mechanical stirring. As a comparison, melt of different amounts of Si_3N_4 are also prepared(40 mg, 80 mg, 150 mg into the 2 g Li melt).

Preparation of polyaniline modified carbon cloth (PMCC): The PMCC was achieved by the modified method. Firstly, the carbon cloth was hydrophilic treated. The carbon cloth was soaked in aqua regia at 40 ºC for 12 hours and wash and dry. The obtained acid-treated carbon cloth is to make the surface of the carbon cloth generate defects so as to facilitate the polymerization of polyaniline on the surface of carbon cloth (A-CC). Secondly, 1.2 ml aniline monomer was added into 25 ml phytic acid solution (50%) to form solution A. And 1 g ammonium persulfate (APS) was added into 30 mL 4 °C deionized water to form solution B. Finally, solution A and solution B are mixed and stirred rapidly, and polyaniline was deposited on carbon cloth by interfacial polymerization at 4 °C. The obtained polyaniline-coated carbon cloth was carbonized at 800 °C for 2 hours by heating rate 2 ºC /min under Ar atmosphere and named as ***PMCC***. The mass of the carbon cloth is about 13 mg.

Melt infiltration of DLi/LiSi$_x$ into the PMCC scaffold (DLi/LiSi$_x$ CA): The infusion process of DLi/LiSi$_x$ alloy melt into 3D PMCC disc was performed in the glovebox under Ar protection (O_2, H_2O<0.1ppm). The prepared DLi/LiSi$_x$ alloy melt still remained at 300 °C. PMCC was dipped into the DLi/LiSi$_x$ melt. Then, the DLi/LiSi$_x$ melt infused into PMCC and the whole scaffold was coated with DLi/LiSi$_x$. Finally, DLi/LiSi$_x$ composite anode (DLi/LiSi$_x$ CA) lithium metal anode was obtained. As a control, pure lithium was compounded to PMCC at a higher temperature (450°C, this is because the undoped lithium metal cannot easily be absorbed by the carbon cloth at the same temperature.) by the same melt perfusion method (Li-CC). The samples prepared with different DLi/LiSi$_x$ melt are called ***DLi/LiSi$_x$ CA-40***, ***DLi/LiSi$_x$ CA-80***, ***DLi/LiSi$_x$ CA-150.*** Meanwhile, the samples mentioned ***DLi/LiSi$_x$ CA*** in the original text are ***DLi/LiSi$_x$ CA-40.*** The mass of the whole electrode is about 30 mg, ***DLi/LiSi$_x$*** loading is 17 mg.

Material Characterizations: The scanning electron microscope (SEM) images are obtained by Zeiss SIGMA 500. X-ray powder diffraction (XRD) (Bruker Scientific Instruments Hong Kong CO., Limited, D8 Advance) are characterized Cu Kα radiation (λ= 1.5418 Å) in the 2θ degrees ranged from 20° to 90°. The elemental component and valence state of as-prepared products are analyzed by X-ray photoelectron spectroscopy (PHI QUANTERA-II SXM, Al Target, 1486.6eV, line width 0.68eV).

Electrochemical Measurements: The symmetric cells are fabricated with 2025 coin-type cells in a glove box with the O_2 and H_2O content under 0.1 ppm. pure Li foil, Li-CC and DLi/LiSi$_x$ CA is used 1.0M LiTFSI in DME: DOL=1:1 Vol%. The cells are cycled using galvanostatic charge-discharge method at various current densities with a LANHE CT2001A battery test system. The electrochemical impedance spectroscopy tests are carried out in a frequency range from 0.01 Hz to 100 kHz with 5 mV amplitude.

Theoretical calculation: The Forcite module, which runs on Materials Studio 8, models Li atom adsorption on graphite and atom-doped graphite. Algorithm set to smart and Max. iterations set to 5000. Forcefield set to compass. Different main crystal planes of $LiSi_2N_3$ have different adsorption energies on graphite. The adsorption energies for Li atoms ($LiSi_2N_3$ molecules) on these fragments are calculated using the formula: $E = E_{total}-E_G-E_{Li}$, where E is the adsorption energy of the lithium atom on the corresponding surfaces, E_G is the energy of the graphene (or heteroatom doped graphene), E_{Li} is the energy of one isolated lithium atom ($LiSi_2N_3$ molecules). E_{tol} is the energy of the optimized structures for lithium atom ($LiSi_2N_3$ molecules) adsorbed on the graphene planes (or heteroatom doped graphene). (110), (111) and (151) crystal plane of $LiSi_2N_3$ are adopted for calculate interaction between slabs and graphite.

Measurement of the Li$^+$ transference number: The Li^+ transference number (t_{Li+}) was determined using the potentiostatic polarization method using a CHI 6081D (ShangHai ChenHua) at an applied voltage polarization of 0.01 V. The polarization of Li||Li, Li-CC ||Li-CC and DLi/LiSi$_x$ CA || DLi/LiSi$_x$ CA symmetric cells and their serial Nyquist plots before and after polarization are used to calculate t_{Li+} based on following **Equation *(S1)***: $t_{Li+}=[I_s(\Delta V-I_0R_0)]/([I_0(\Delta V-I_sR_s)])$

The initial and steady-state currents are I_0 and I_s, respectively. The interfacial resistances before and after polarization are R_0 and R_s, respectively. And ΔV is the applied potential (= 0.01 V).

Measurement of electronic conductivity: To measure the electronic conductivity of DLi/LiSi$_x$ CA, Li-CC and Li, a direct current (5 mA) is applied to the cells assembled with DLi/LiSi$_x$ CA, Li-CC and Li sandwiched between two stainless steel (SS) blocking electrodes. The electronic conductivity was calculated following ***Equation (S2)***:$\sigma_e = 1/\rho = L/R \times S = I \times L/U \times S$ where ρ is the electrical resistivity, σ_e is the electronic conductivity, U is the average voltage increase, I is the applied current of 5 mA, S is the contact area between SS and anode, and L is the anode thickness.

Measurement of Li$^+$ diffusion coefficient: The sequential CV curves are measured with different scan rates (0.1, 0.2, 0.3, 0.4, 0.5, and 0.6 mV s^{-1}) within the voltage range of 2.7-4.3 V (NCM 811||DLi/LiSi$_x$ CA cell), 3.6-4.9 V (LNMO|| DLi/LiSi$_x$ CA cell) and 2.5-3.5V (LFP||DLi/LiSi$_x$ CA cell). From the CV curves, the Li$^+$ diffusion coefficient (D_{Li+}) is calculated using the Randles-Sevcik equation ***(Equation S3):*** $I_{peak}=2.69\times10^5 n^{1.5} A D_{Li+}^{0.5} C_{Li+} v^{0.5}$

Equation S3 shows the linear relationship between the peak current (I_{peak}) and the square root of the CV scan rate ($v^{0.5}$). where n is the number of electrons transferred, A is the surface area of the electrode, C_{Li+} is the Li$^+$ concentration in the liquid electrolyte, and v is the voltage scan rate.

***Theoretical specific capacity*：**According to the quality of the electrode. And the practical specific capacity of graphite is 340 mAh g^{-1}. The silicon content of silicon nitride is 60%(Silicon theoretical specific capacity: 3590 mAh g^{-1}). Lithium metal theoretical specific capacity: 3860 mAh g^{-1}. Theoretical specific capacity is calculated based on the mass ratio of PMCC, Si and Li metal. Theoretical specific capacity=2315.7 mAh g^{-1}

Supplementary Figures

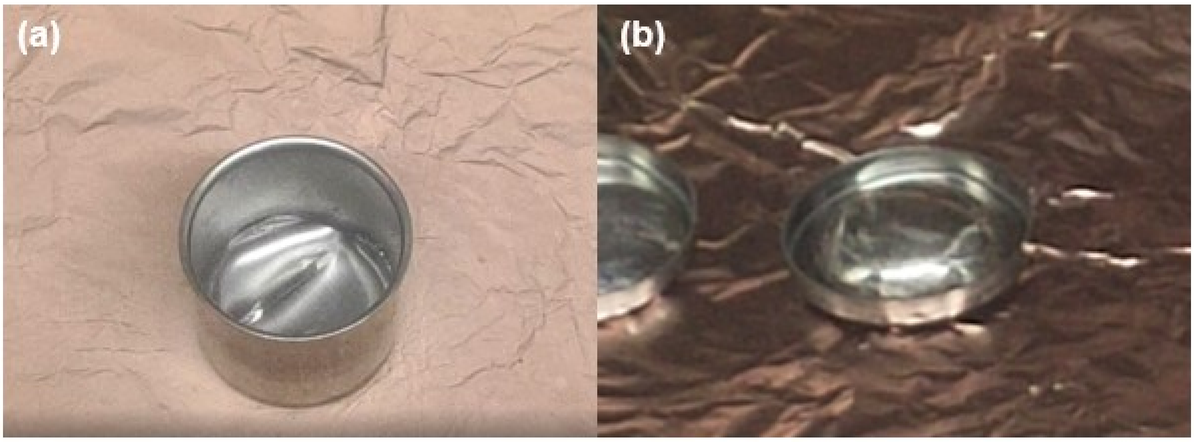

Figure S1. The digital photos show (a) Stirred molten DLi/LiSi$_x$ melt and (a) molten pure lithium.

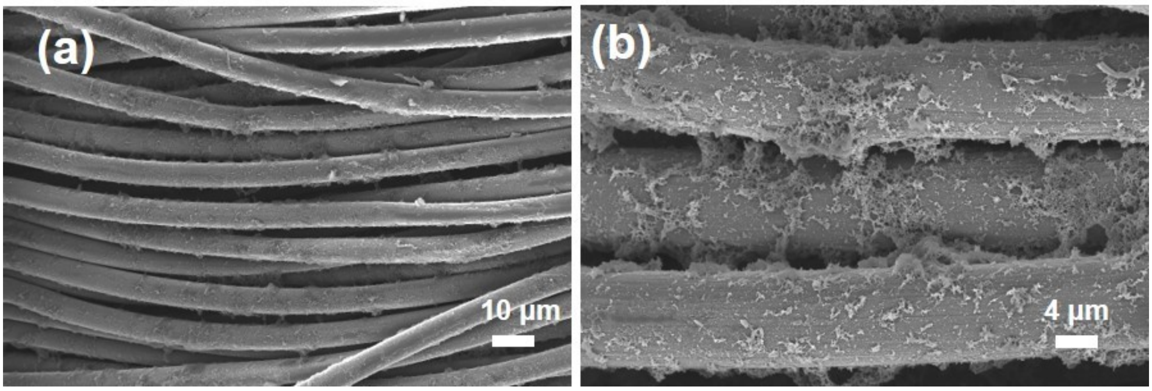

Figure S2. (a) Low magnification and (b) Medium magnification SEM image of PMCC.

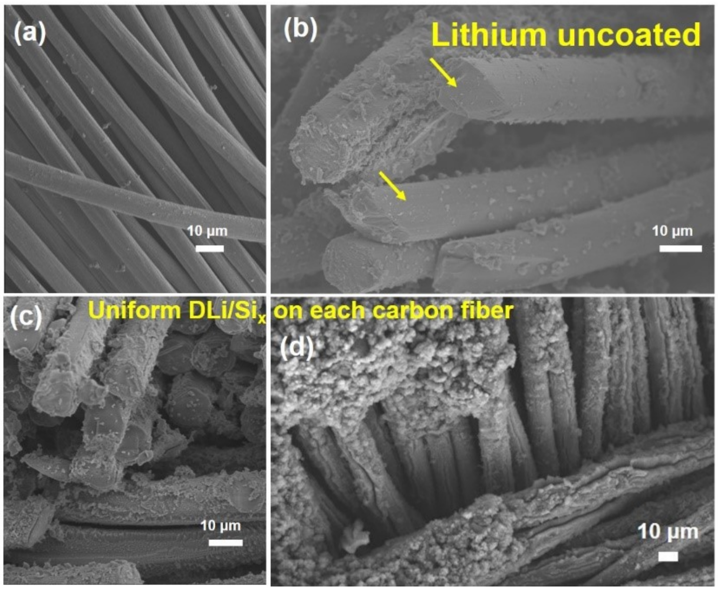

Figure S3. (a) Magnification of A-CC (b) High magnification SEM image of Li-CC anode. (c) Low and (d) high magnification SEM image of DLi/LiSi$_x$ CA.

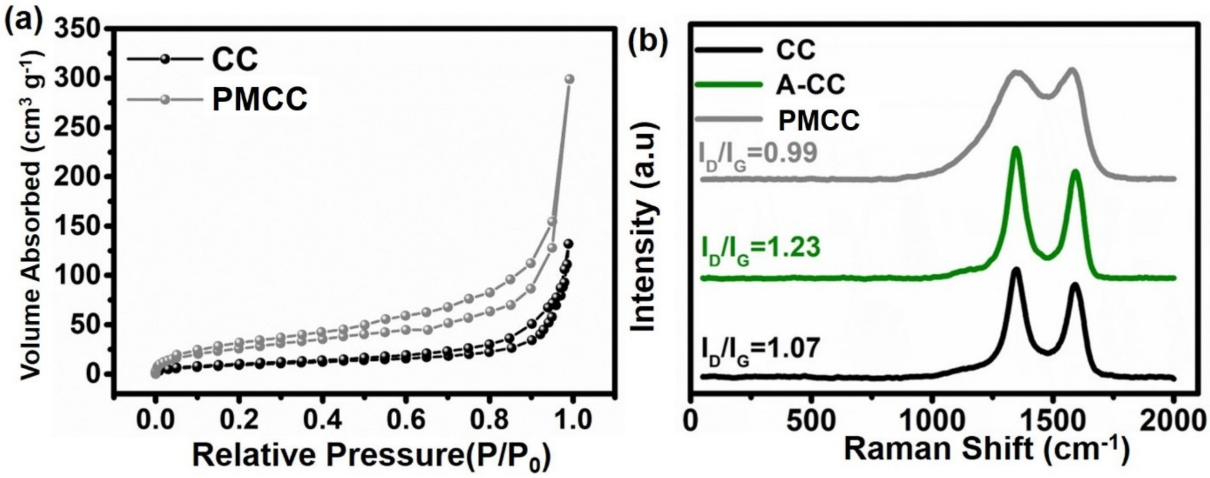

Figure S4. (a) N_2 adsorption-desorption isotherms for CC and PMCC. and Raman (c) spectrum for CC, A-CC and PMCC.

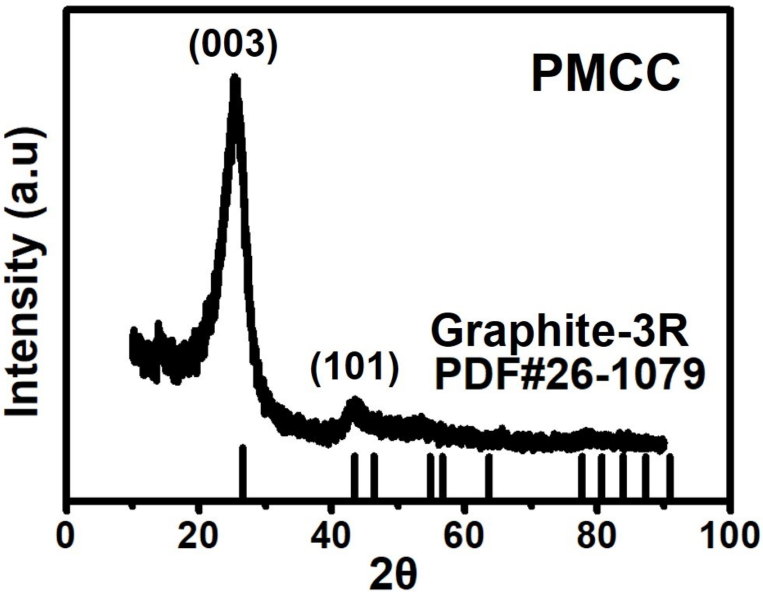

Figure S5. XRD patterns of PMCC.

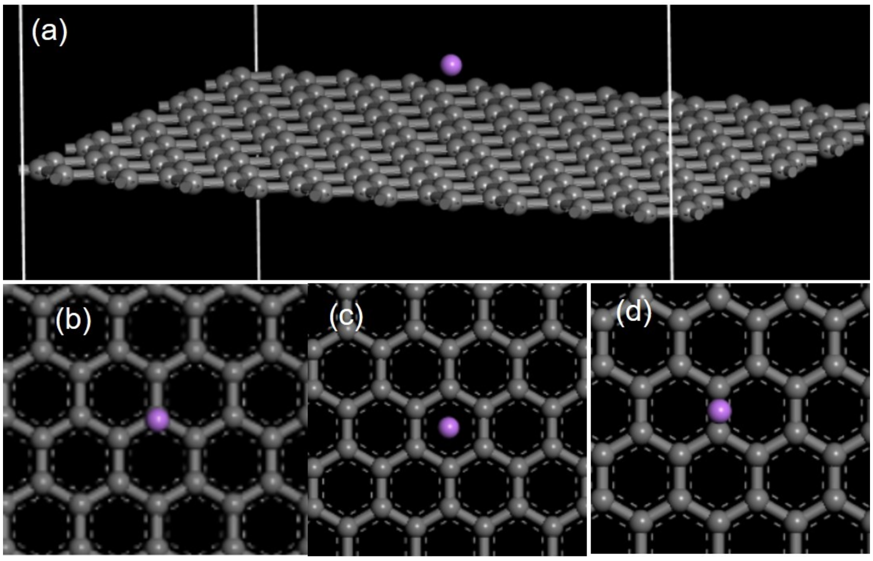

Figure S6. (a) Schematic diagram of a lithium atom on the surface of graphite. Three main positions of lithium atoms on the surface of graphite (b)Top (c) Hollow and (d) Bridge.

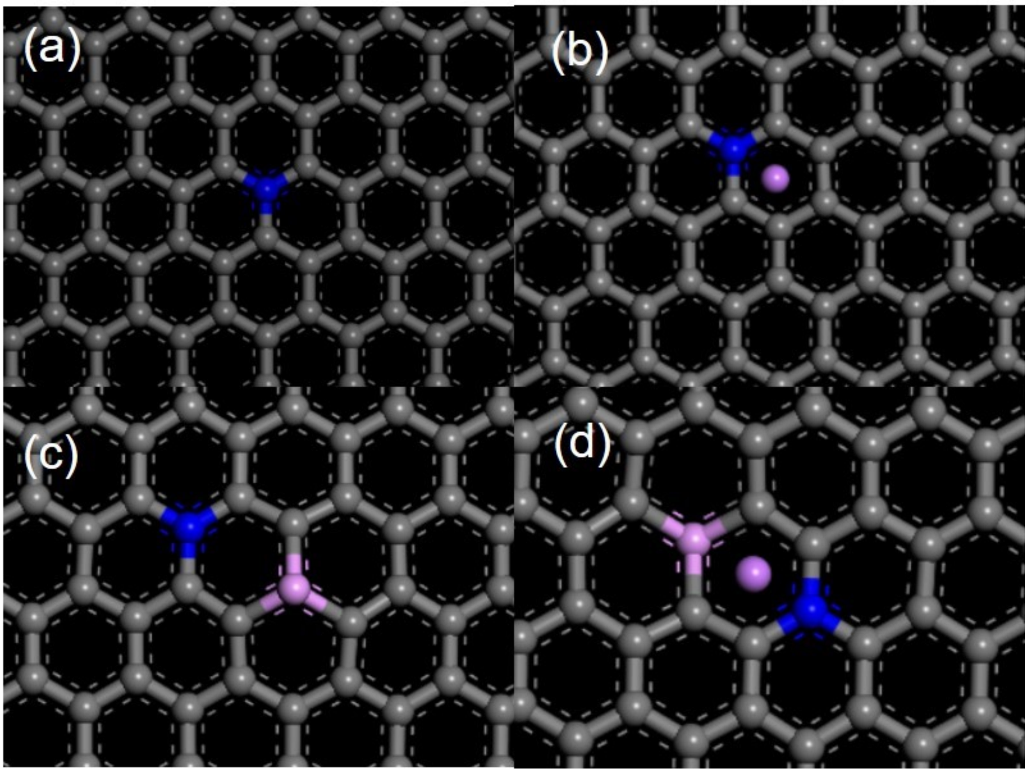

Figure S7. (a) Nitrogen doped graphite (b) Hollow Li on nitrogen doped graphite (c) Nitrogen phosphorus co-doped graphite (d) Hollow Li nitrogen phosphorus co-doped graphite

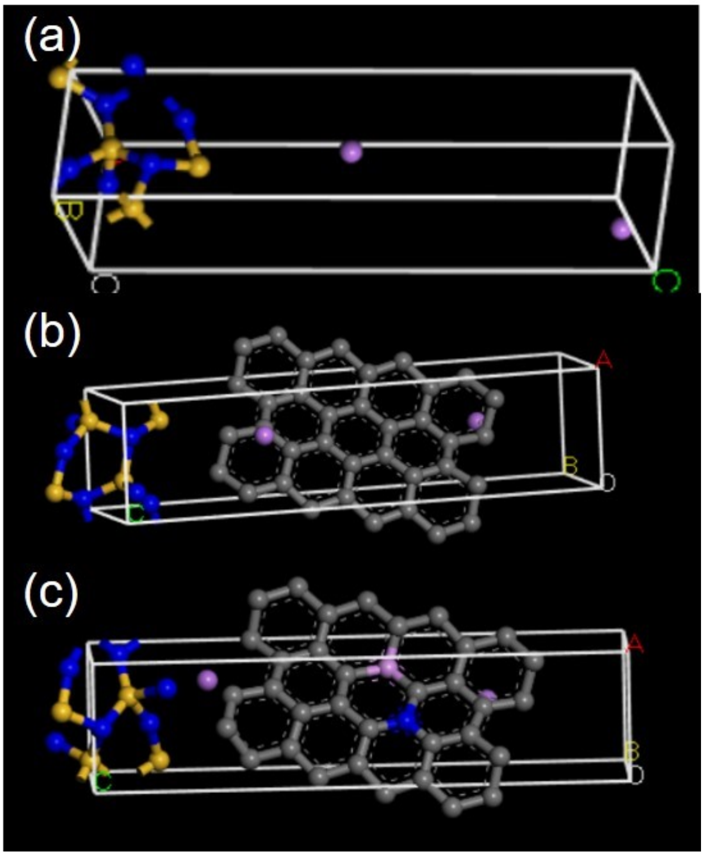

Figure S8. (a) Constructed surface structure, vacuum layer 15 Å $LiSi_2N_3$ (1 1 0) Crystal plane. (b) Optimized $LiSi_2N_3$ (1 1 0)- graphite. (c) Optimized $LiSi_2N_3$ (1 1 0)- N, P graphite.

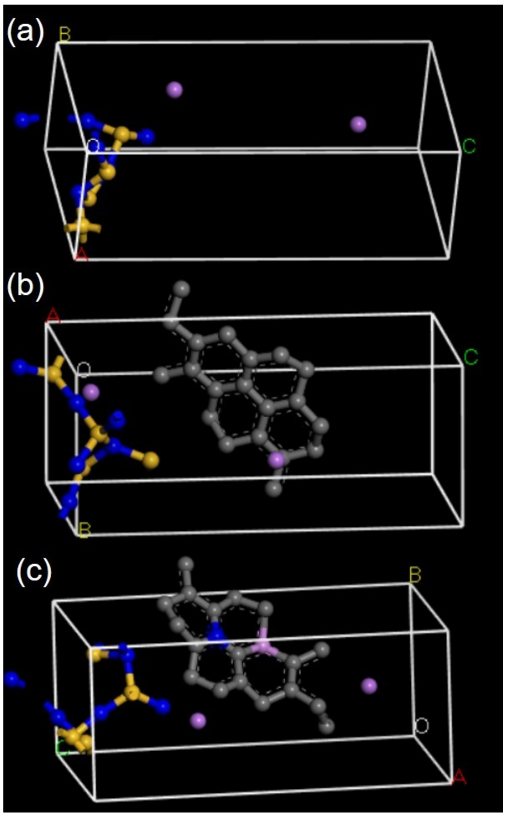

Figure S9. (a) Constructed surface structure, vacuum layer 15 Å $LiSi_2N_3$ (1 1 1) Crystal plane. (b) Optimized $LiSi_2N_3$ (1 1 1)- graphite. (c) Optimized $LiSi_2N_3$ (1 1 0)- N, P graphite.

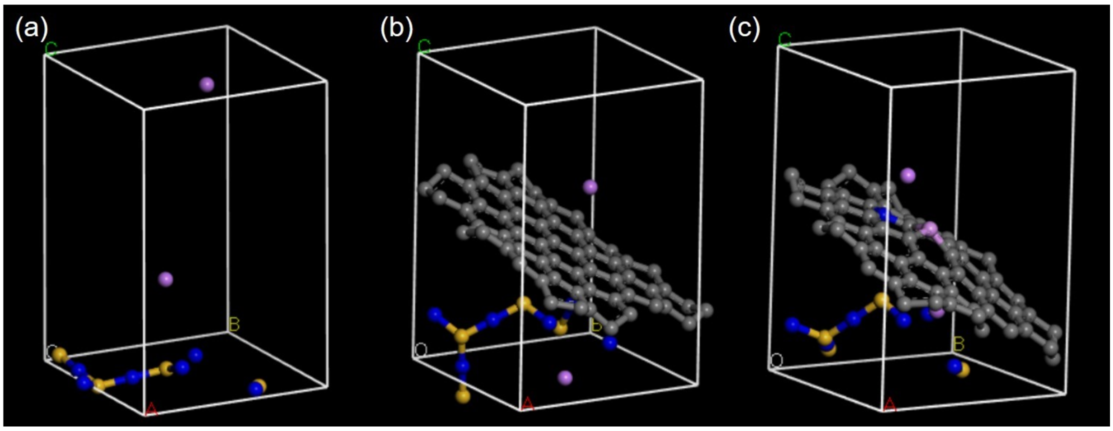

Figure S10. (a) Constructed surface structure, vacuum layer 15 Å $LiSi_2N_3$ (1 5 1) Crystal plane. (b) Optimized $LiSi_2N_3$ (1 5 1)- graphite. (c) Optimized $LiSi_2N_3$ (1 5 1)- N, P graphite.

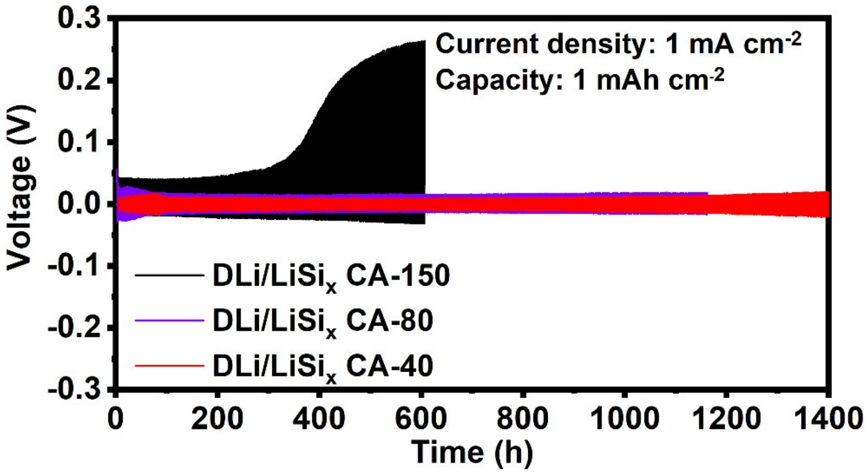

Figure S11. Electrochemical performance of symmetric cells with different amounts of Si_3N_4.

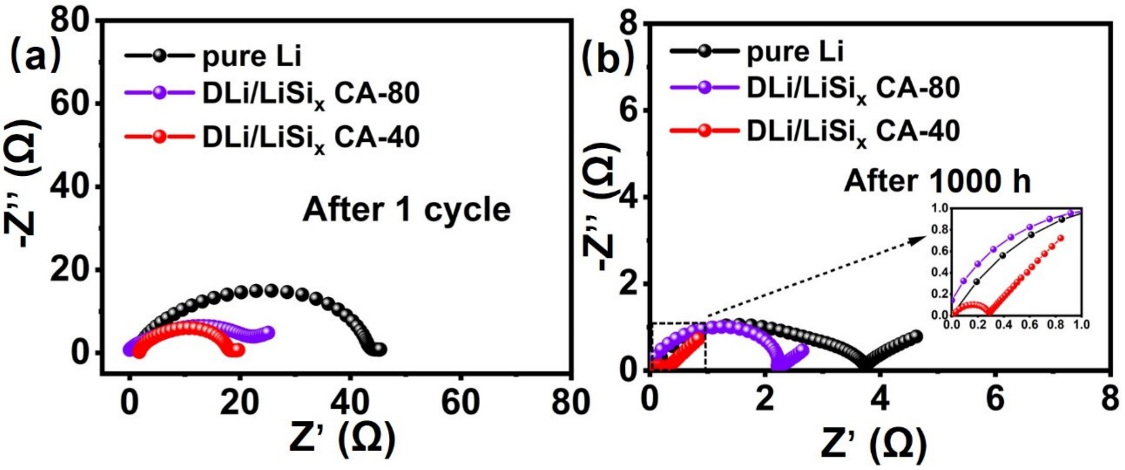

Figure S12. EIS plots of the symmetric batteries (a) after 1 cycle and (f) after 1000 h based on Li||Li, DLi/$LiSi_x$ CA-80 and DLi/$LiSi_x$ CA-40 symmetric cells.

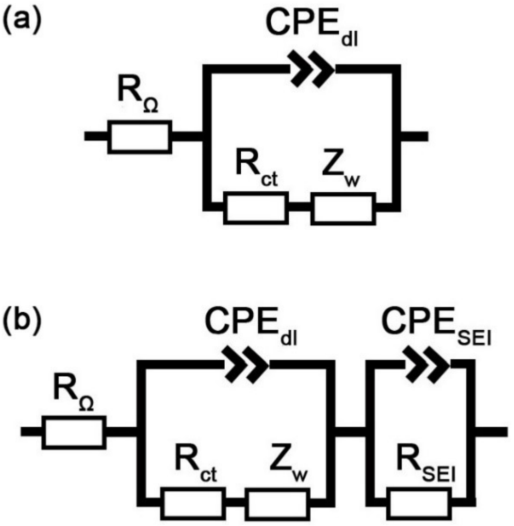

Figure S13. (a) Equivalent circuit model for the DLi/$LiSi_x$ CA before and (b) after cycles

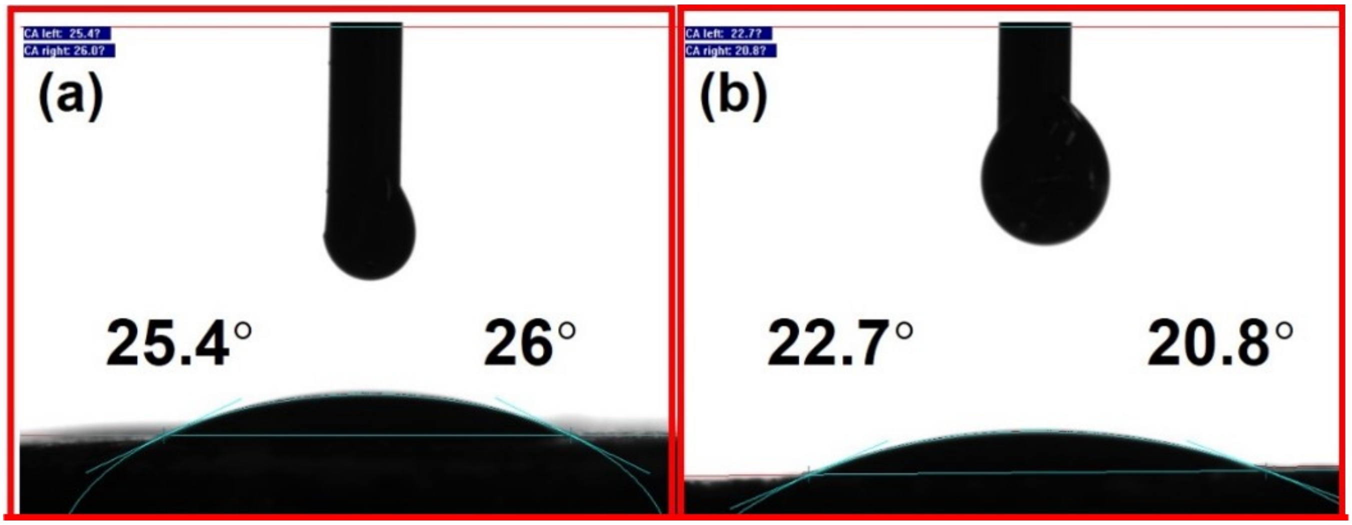

Figure S14. Photographs of electrolyte droplet placed onto the surface of (a) pure Li and (b) DLi/LiSi$_x$ CA.

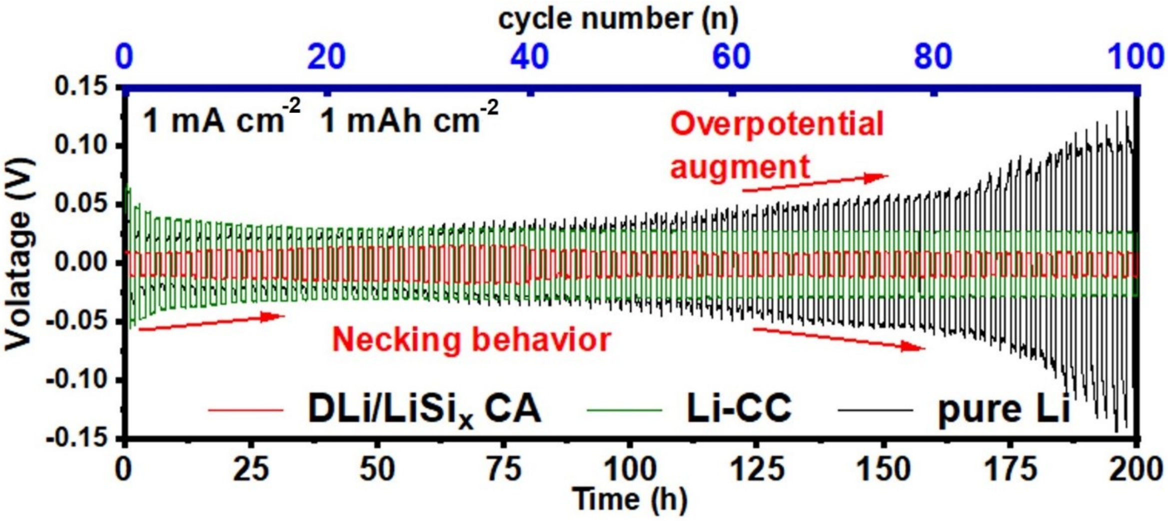

Figure S15. Magnified voltage profile of the symmetrical battery during the first 200 h cycling corresponding to Figure 4a.

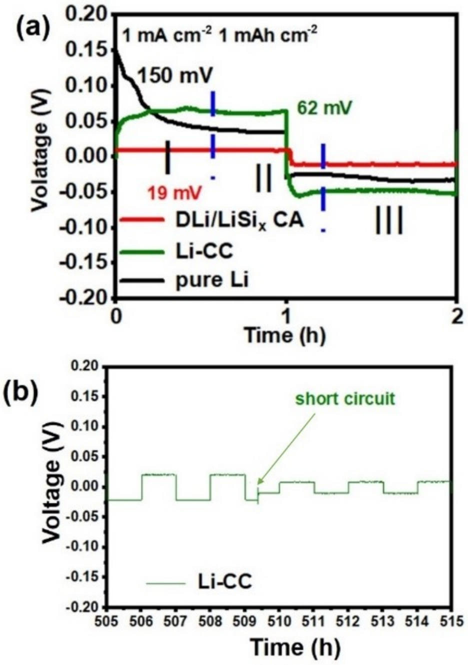

Figure S16. (a) Detailed voltage profiles of Li||Li, Li-CC||Li-CC and DLi/LiSi$_x$ CA|| DLi/LiSi$_x$ CA cells during the first Li stripping/plating process (b) Short circuit enlarged view for Li-CC symmetrical cell in 509 cycles (corresponding to Figure 4a).

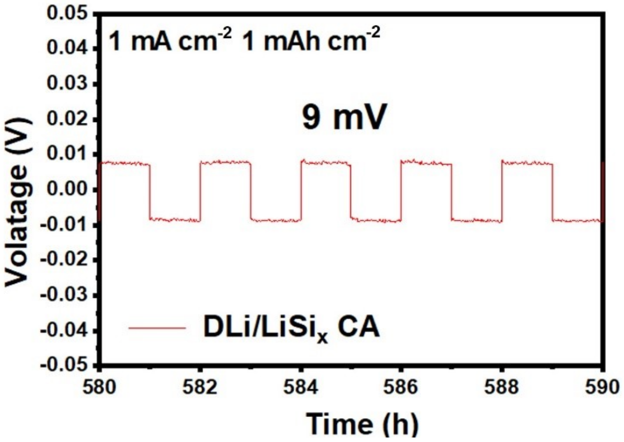

Figure S17. Area of minimum overpotential for DLi/LiSi$_x$ CA|| DLi/LiSi$_x$ CA symmetrical cells (corresponding to Figure 4a).

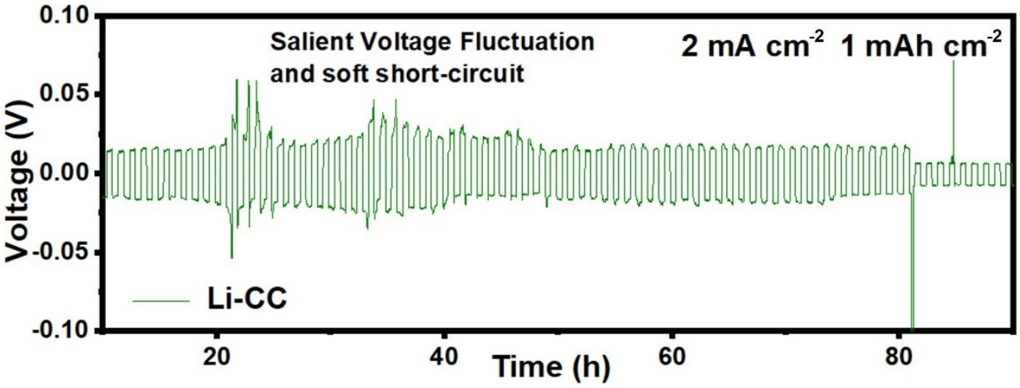

Figure S18. Area 10 h-90 h of overpotential for Li-CC|| Li-CC symmetrical cells **(corresponding to Figure 4b)**.

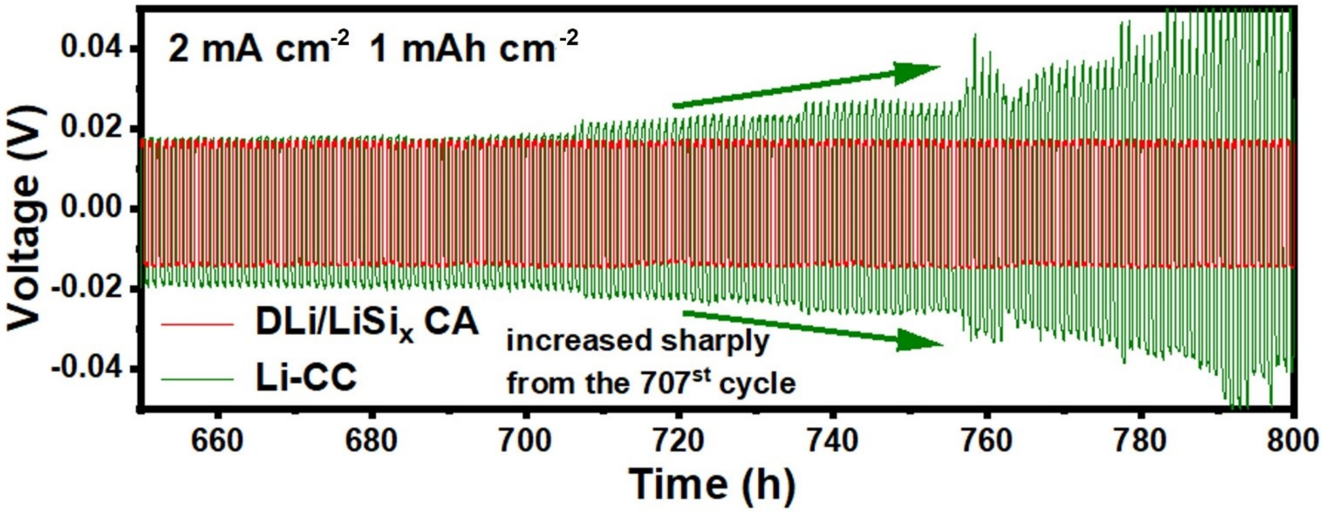

Figure S19. Area 650 h-800 h of overpotential for Li-CC|| Li-CC symmetrical cells **(corresponding to Figure 4b)**.

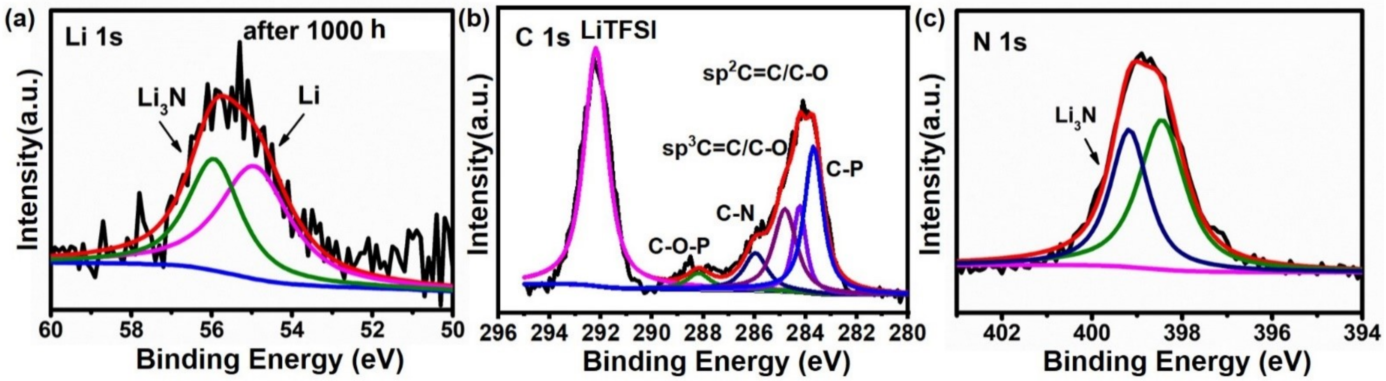

Figure S20. XPS survey spectrum of DLi/LiSi$_x$ CA after 1000 h.

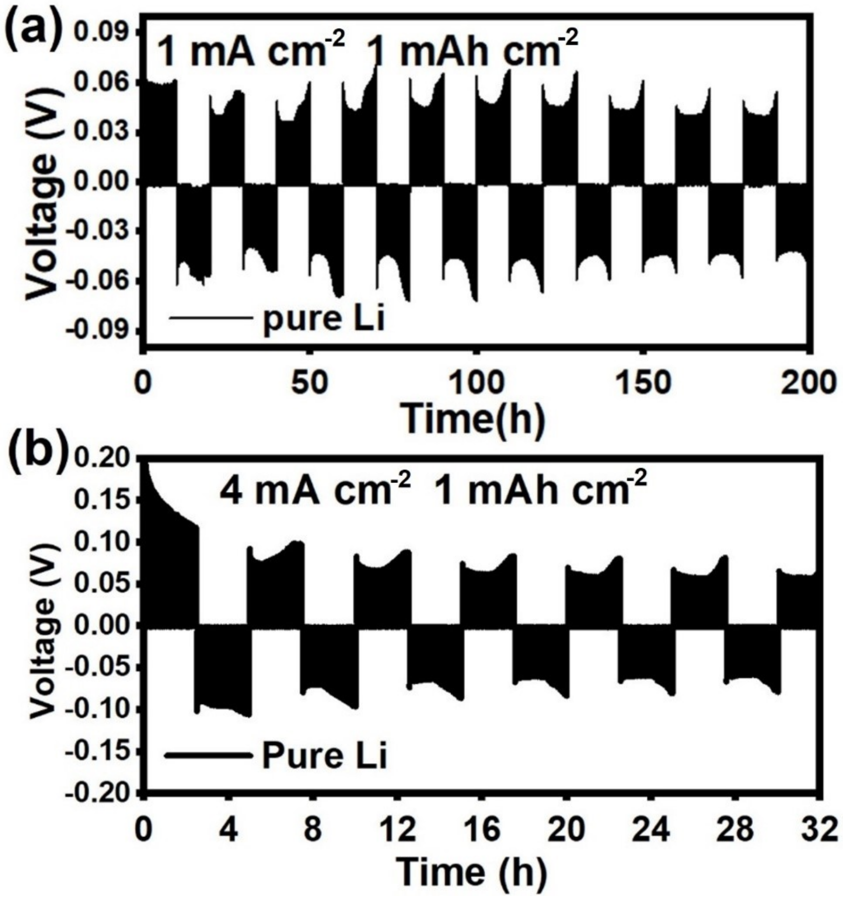

Figure S21. GITT voltage profiles combined with the previous galvanostatic profiles in Li||Li (a) 1 mA cm^{-2} (b) 4 mA cm^{-2}.

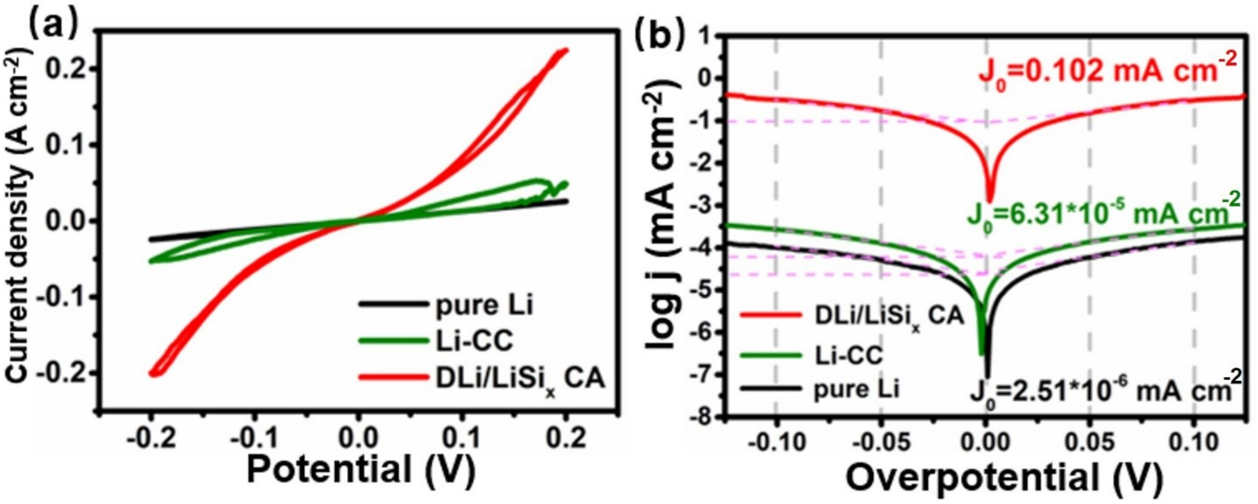

Figure S22. (a) Cyclic voltammetry (CV) spectra in the range of -0.2 V to 0.2 V at 0.1 mV s $^{-1}$ for symmetric cells consisting of Li||Li, Li-CC||Li-CC and DLi/LiSi$_x$ CA|| DLi/LiSi$_x$ CA. (b) Tafel plots of Li||Li, Li-CC||Li-CC and DLi/LiSi$_x$ CA || DLi/LiSi$_x$ CA symmetric cells.

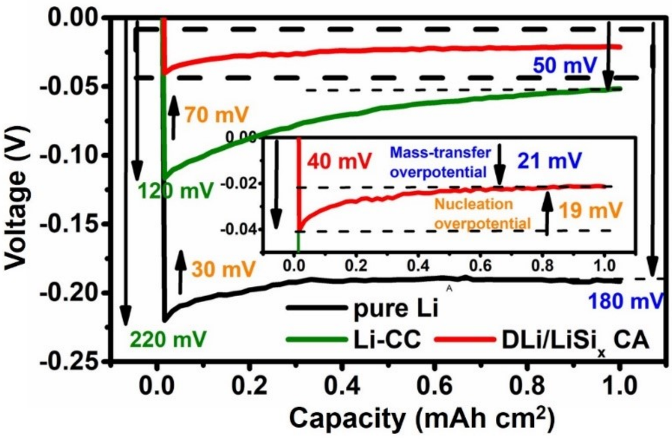

Figure S23. The voltage profiles to estimate nucleation and mass-transfer overpotential of pure Li, Li-CC and DLi/LiSi$_x$ CA.

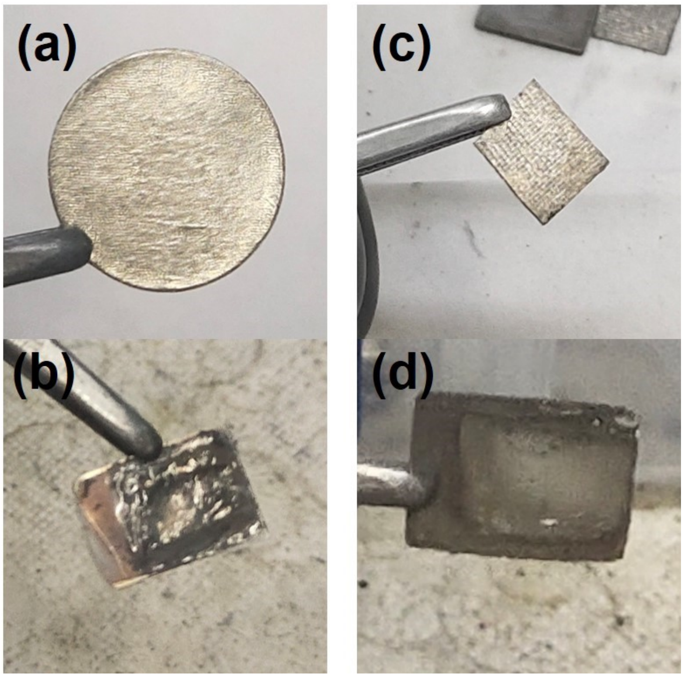

Figure S24. The optical photograph of symmetric cells with (a-b) pure Li electrode and (c-d) DLi/LiSi$_x$ CA. anode before and after cycles.

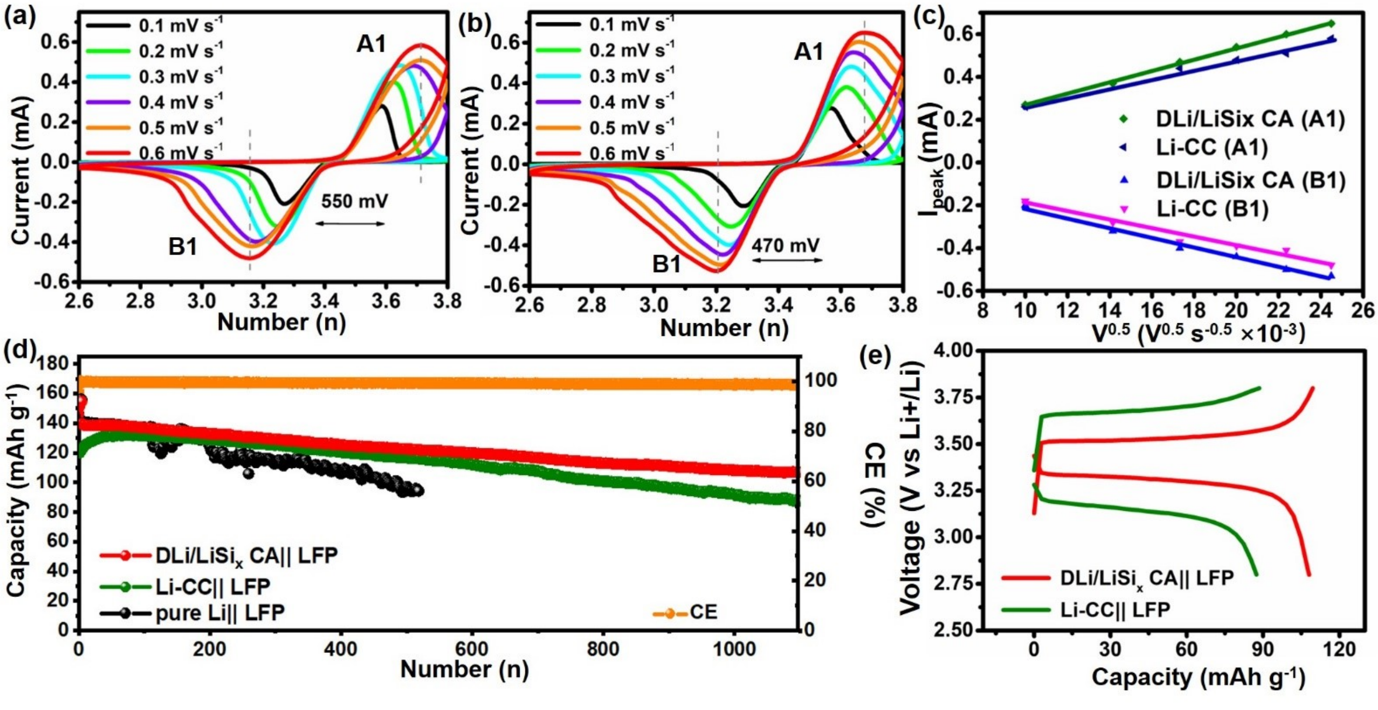

Figure S25. The CV curves of (a) LFP||Li-CC and (b) LFP || DLi/LiSi$_x$ CA full cells at various voltage scan rates (0.1-0.6 mV s^{-1}) in the voltage range of 2.6-3.8 V and (c) The corresponding linear fit of the cathodic/anodic peak current intensities as a function of the square root of the scan rates. (g) Cycling performance of the cells at current rate of 1 C. (Galvanostatic charge/discharge curves of LFP|| Li-CC and LFP|| DLi/LiSi$_x$ CA full cell of the 1000th cycles.)

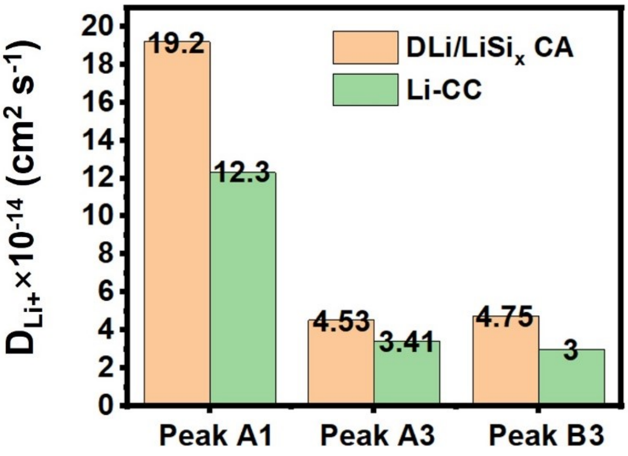

Figure S26. Comparison of Li$^+$ diffusion coefficients of NCM 811 cathode coupled with Li-CC and DLi/LiSi$_x$ CA.

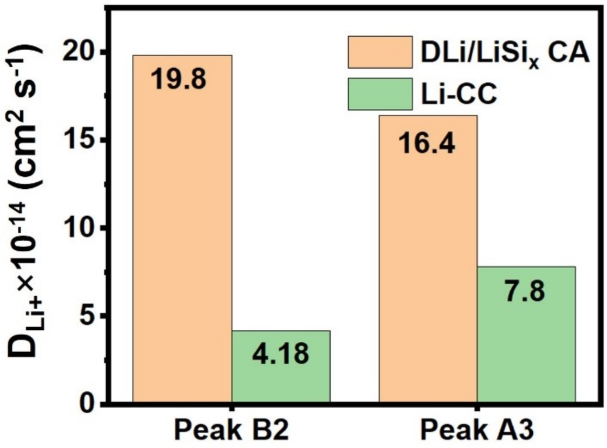

Figure S27. Comparison of Li$^+$ diffusion coefficients of LNMO cathode coupled with Li-CC and DLi/LiSi$_x$ CA.

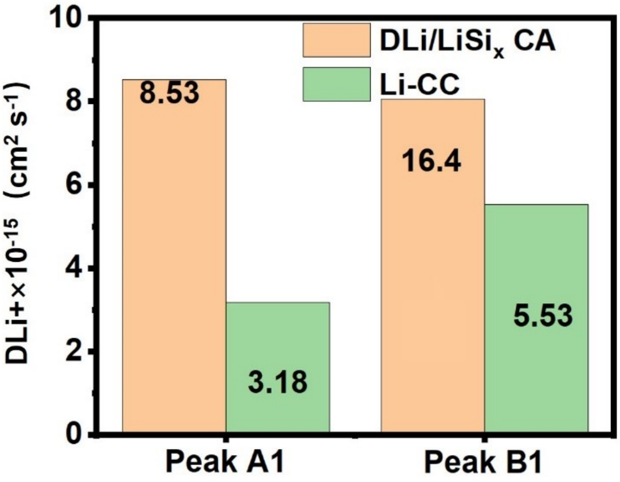

Figure S28. Comparison of Li$^+$ diffusion coefficients of LFP cathode coupled with pure Li-CC and DLi/LiSi$_x$ CA.

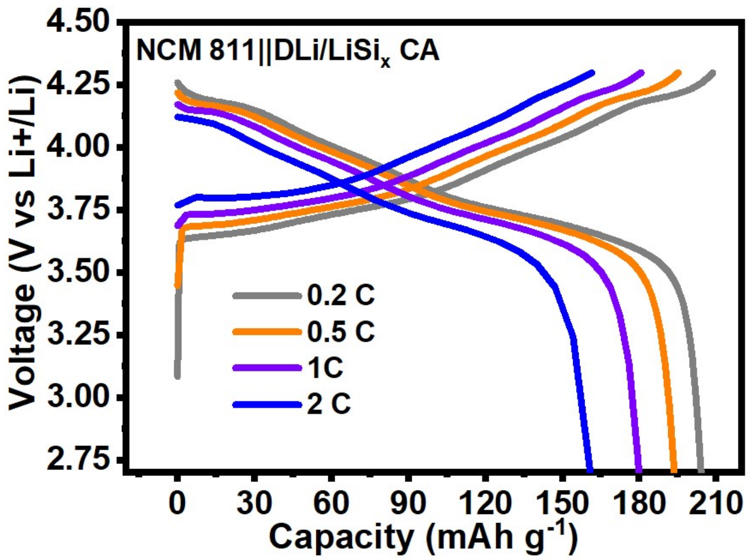

Figure S29. Galvanostatic charge/discharge curves at 0.2 C, 0.5C, 1 C, and 2 C of NCM 811||DLi/LiSi$_x$ CA full cell.

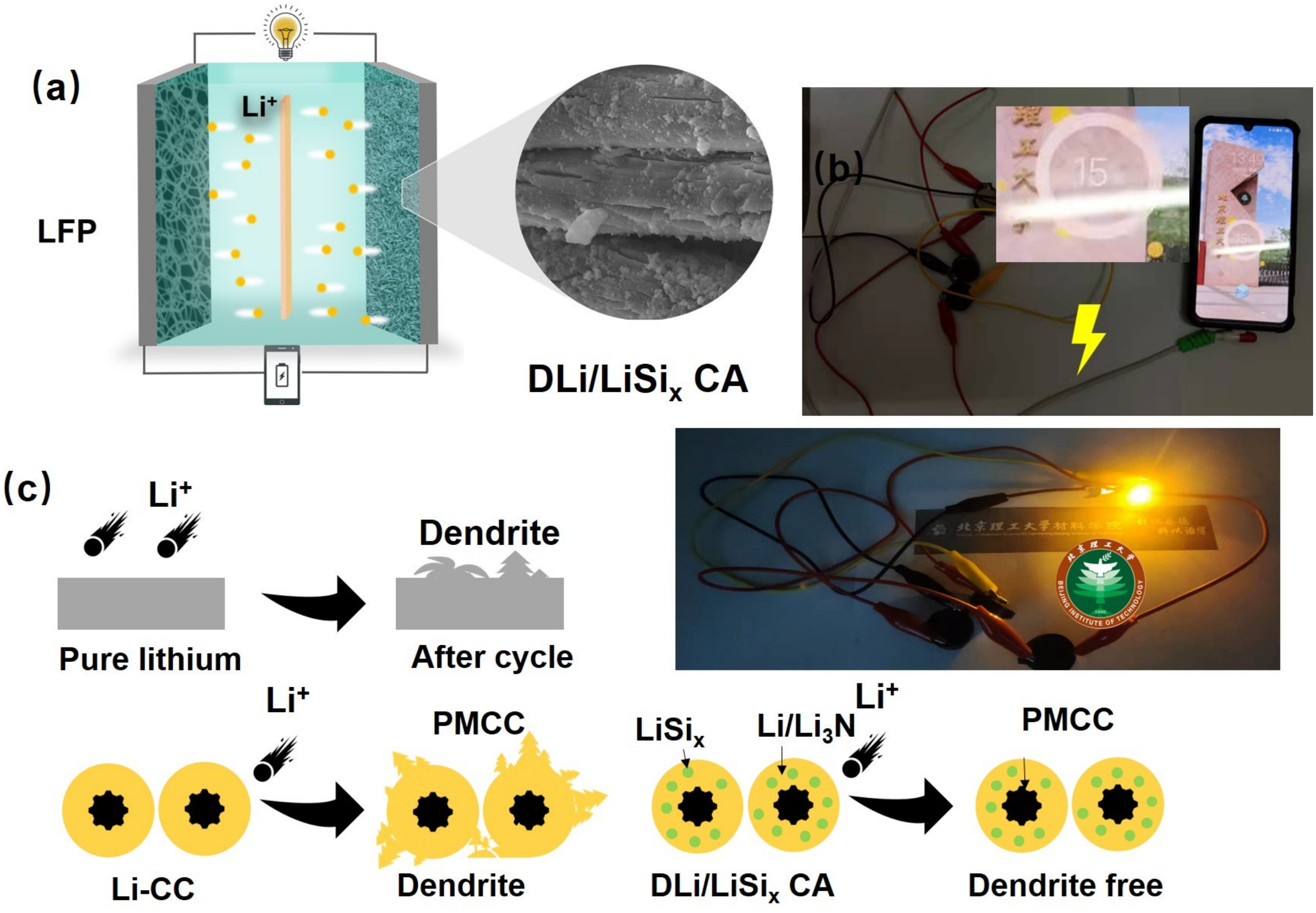

Figure S30. (a) Schematic illustration of the full cell. (b) LFP || DLi/LiSi$_x$ CA full cells can charge the Mobile phone and turn on the LED bulb. (c) Scheme illustrations for the Li nucleation and plating process on the surface of pure Li, Li-CC and DLi/LiSi$_x$ CA.

Supplementary Tables

Table S1. Adsorption energy (E_{total}, kcal/mol) calculated by Forcite module from MS8.

Structure	E_{total} (kcal/mol)	Structure diagram
Li- Top graphite.	-36.6201	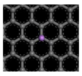
Li- Hollow graphite	-36.6574	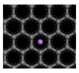
Li- Bridge graphite	-36.6346	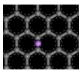
Li- Hollow N doped graphite	-0.10907	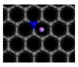
Li- Hollow N, P doped graphite	-36.8174	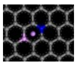
$LiSi_2N_3$ (1 1 0)- graphite	-469.363	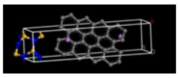
$LiSi_2N_3$ (1 1 0)- N, P doped graphite	-487.873	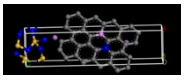
$LiSi_2N_3$ (1 1 1)- graphite	-0.44179	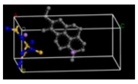
$LiSi_2N_3$ (1 1 1)- N, P doped graphite	-9.62751	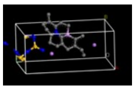
$LiSi_2N_3$ (1 5 1)- graphite	-160.312	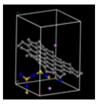
$LiSi_2N_3$ (1 5 1)- N, P doped graphite	-163.272	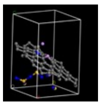

Table S2 EIS parameters of symmetric cells for the pure Li and DLi/LiSi$_x$ CA-40 and DLi/LiSi$_x$ CA-40 electrode, **corresponding to Figure S12**.

Samples	Resistance (Ω)		
	R_Ω	R_{SEI}	R_{ct}
DLi/LiSi$_x$ CA-40 after 1 cycle	1.1	8.73	18
DLi/LiSi$_x$ CA-80 after 1 cycle	1.1	8.82	25
pure Li after 1 cycle	1.57	12.12	42
DLi/LiSi$_x$ CA-40 after 1000h	2.91	4.37	0.5
DLi/LiSi$_x$ CA-80 after 1000h	2.9	5.02	2
pure Li	2.81	7.62	4

Table S3. Comparison of electrochemical cycle performance of the symmetrical battery with DLi/LiSi$_x$ CA infuse Li anode with other reported lithium metal anode.

lithium metal anode	Cycle time	Overpotential	Current density and capacity	Reference
DLi/LiSi$_x$ CA	1400 h	18 mV	1 mA cm^{-2} and 1 mAh cm^{-2}	This work
Li–Si Alloy-Type	1000	14 mv	1 mA cm^{-2} and 1 mAh cm^{-2}	1
C/SiNW/Li composite	600 h	100 mV	1 mA cm^{-2} and 1 mAh cm^{-2}	2
3D Cu nanowire infuse Li anode	200 h	~130 mV	3 mA cm^{-2} and 1 mAh cm^{-2}	3
LRS-modified Li		~40 mV	1 mA cm^{-2} and 1 mAh cm^{-2}	4
3D CCZF@Li	900 h	22 mV	1 mA cm^{-2} and 1 mAh cm^{-2}	5
CoO/nickel foam infused Li composite anode	270 h	~40 mV	1 mA cm^{-2} and 1 mAh cm^{-2}	6
Li-SirGO	100 h	~60 mV	1 mA cm^{-2} and 1 mAh cm^{-2}	7
interconnected graphene framework/Li anode	200 h	~60 mV	2 mA cm^{-2} and 1 mAh cm^{-2}	8
Li/Si/ZnO (LiSZ) composite anode	1000	~25 mV	1 mA cm^{-2} and 1 mAh cm^{-2}	9
Li coated carbonized eggplant anode	50 h	480 mV	10 mA cm^{-2} and 1 mAh cm^{-2}	10
cucumber-like lithiophilic composite skeleton@Li	2000	20 mV	1 mA cm^{-2} and 1 mAh cm^{-2}	11
Si-O-Si membrane	1000	~20 mV	0.5 mA cm^{-2} and 1 mAh cm^{-2}	12
silicon (Si) coating onto the polypropylene (PP) separator	1000	~78.9	0.5 mA cm^{-2} and 1 mAh cm^{-2}	13
3D N graphitic carbon sponge/Li anode	320 h	20 mV	0.5 mA cm^{-2} and 0.5 mAh cm^{-2}	14
carbon felt-Cu loading Li	1000 h	~50 mV	1 mA cm^{-2} and 1 mAh cm^{-2}	15

Li coated Si-vertical graphene host	200 h	350 mV	1 mA cm^{-2} and 1 mAh cm^{-2}	16
ZnO/carbon framework/Li anode	390 h	~20 mV	1 mA cm^{-2} and 1 mAh cm^{-2}	17
graphene nanowall/Li composite anode	350 h	29 mV	1 mA cm^{-2} and 1 mAh cm^{-2}	18
3D Si@carbon nanofibers (CNFs) @ZnO-ZnO-Cu skeleton (SCZ)	900 h	~14 mV	1 mA cm^{-2} and 1 mAh cm^{-2}	19
carbon nanofibers scaffold infused Li	200 h	60 mV	1 mA cm^{-2} and 1 mAh cm^{-2}	20
Li_2C_2 alloy nanosheets composed	800 h	~ 30mV	1 mA cm^{-2} and 1 mAh cm^{-2}	21
Li/carbon nanotube	2000 h	from 89 to 54 mV	40 mA cm^{-2} and 2 mAh cm^{-2}	22
Lithiophilic COF-LZU1 microspheres	400 h	~25 mV	1 mA cm^{-2} and 1 mAh cm^{-2}	23
VGCF	860 h	-	average coulombic efficiency of 99.36% in 1 mA cm^{-2} and 1 mAh cm^{-2}	24
layer-by-layer assembled atomic distributed Si/C	400 h	~24 mV	1 mA cm^{-2} and 1 mAh cm^{-2}	25

Table S4. Initial (I_0) / steady-state (I_s) currents corresponding to Li$^+$ transference numbers (t_{Li+}) and bulk and interfacial resistances fitted by Nyquist plots before/after polarization.

Bulk Anode	R_0(Ω)	R_s(Ω)	I_0(mA)	I_s(mA)	t_{Li+}
Pure Li	54	102	0.084	0.061	0.529095
Li-CC	26	50	0.243	0.067	0.520731
DLi/LiSi$_x$ CA	13	22	1	0.176	0.591983

Table S5. Based on the linear fit's slope, the calculated D_{Li+} values for the full cell, **corresponding to Figure S26-S28**.

D_{Li+} values	A1(cm^2 s^{-1})	A3(cm^2 s^{-1})	B3(cm^2 s^{-1})
NCM811|| DLi/LiSi$_x$ CA	19.2×10^{-14}	4.53×10^{-14}	4.75×10^{-14}
NCM 811|| Li-CC	12.3×10^{-14}	3.41×10^{-14}	3.0×10^{-14}

D_{Li+} values	A3(cm^2 s^{-1})	B2(cm^2 s^{-1})
LNMO|| DLi/LiSi$_x$ CA	16.4×10^{-14}	19.8×10^{-14}
LNMO|| Li-CC	7.8×10^{-14}	4.18×10^{-14}

D_{Li+} values	A1(cm^2 s^{-1})	B1(cm^2 s^{-1})
LFP|| DLi/LiSi$_x$ CA	8.53×10^{-15}	8.06×10^{-15}
LFP|| Li-CC	3.18×10^{-15}	5.53×10^{-15}

References

1 J. B. Park, C. Choi, S. Yu, K. Y. Chung and D. W. Kim, *Adv. Energy Mater.*, 2021, **2101544**, 1–14.

2 P. Zhang, C. Peng, X. Liu, F. Dong, H. Xu, J. Yang and S. Zheng, *ACS Appl. Mater. Interfaces*, 2019, **11**, 44325–44332.

3 K. R. Adair, M. Iqbal, C. Wang, Y. Zhao, M. N. Banis, R. Li, L. Zhang, R. Yang, S. Lu and X. Sun, *Nano Energy*, 2018, **54**, 375–382.

4 L. Cao, X. Cheng, H. Xu, G. Cao, J. Hu and G. Shao, *J. Mater. Sci. Technol.*, 2021, **76**, 156–165.

5 Y. Li, Y. Wang, Y. Shi, H. Wu, J. Zeng, H. Bu, M. Zhu, C. Xiao, Y. Zhang, G. Gao and S. Ding, *Sci. Bull.*, 2020, **65**, 1094–1102.

6 X. Y. Yue, W. W. Wang, Q. C. Wang, J. K. Meng, Z. Q. Zhang, X. J. Wu, X. Q. Yang and Y. N. Zhou, *Energy Storage Mater.*, 2018, **14**, 335–344.

7 H. Wang, X. Cao, H. Gu, Y. Liu, Y. Li, Z. Zhang, W. Huang, H. Wang, J. Wang, W. Xu, J. G. Zhang and Y. Cui, *ACS Nano*, 2020, **14**, 4601–4608.

8 X. Nie, A. Zhang, Y. Liu, C. Shen, M. Chen, C. Xu, Q. Liu, J. Cai, A. Alfaraidi and C. Zhou, *Energy Storage Mater.*, 2019, **17**, 341–348.

9 C. Ni, J. Mao, Z. Cheng, P. Pan, L. Jiang, Z. Wang, M. Zhang, Y. Zhang, Y. Xing, Y. Zeng, Q. Chen and Y. Hu, *J. Alloys Compd.*, , DOI:10.1016/j.jallcom.2021.160188.

10 H. Wang, D. Lin, J. Xie, Y. Liu, H. Chen, Y. Li, J. Xu, G. Zhou, Z. Zhang, A. Pei, Y. Zhu, K. Liu, K. Wang and Y. Cui, *Adv. Energy Mater.*, 2019, **9**, 1–8.

11 T. Liu, J. Wang, Y. Xu, Y. Zhang and Y. Wang, *Nano-Micro Lett.*, 2021, **13**, 1–13.

12 Z. Wen, W. Fang, L. Chen, Z. Guo, N. Zhang, X. Liu and G. Chen, *Adv. Funct. Mater.*, 2021, **2104930**, 1–11.

13 X. Chen, R. Zhang, R. Zhao, X. Qi, K. Li, Q. Sun, M. Ma, L. Qie and Y. Huang, *Energy Storage Mater.*, 2020, **31**, 181–186.

14 G. Hou, X. Ren, X. Ma, L. Zhang, W. Zhai, Q. Ai, X. Xu, L. Zhang, P. Si, J. Feng, F. Ding and L. Ci, *J. Power Sources*, 2018, **386**, 77–84.

15 X. Y. Yue, X. L. Li, W. W. Wang, D. Chen, Q. Q. Qiu, Q. C. Wang, X. J. Wu, Z. W. Fu, Z. Shadike, X. Q. Yang and Y. N. Zhou, *Nano Energy*, 2019, **60**, 257–266.

16 Y. J. Zhang, S. F. Liu, X. L. Wang, Y. Zhong, X. H. Xia, J. B. Wu and J. P. Tu, *J. Power Sources*, 2018, **374**, 205–210.

17 L. Wang, X. Zhu, Y. Guan, J. Zhang, F. Ai, W. Zhang, Y. Xiang, S. Vijayan, G. Li, Y. Huang, G. Cao, Y. Yang and H. Zhang, *Energy Storage Mater.*, 2018, **11**, 191–196.

18 Z. Hu, Z. Li, Z. Xia, T. Jiang, G. Wang, J. Sun, P. Sun, C. Yan and L. Zhang, *Energy Storage Mater.*, 2019, **22**, 29–39.

19 L. Zhang, H. Zheng, B. Liu, Q. Xie, Q. Chen, L. Lin, J. Lin, B. Qu, L. Wang and D. L. Peng, *J. Energy Chem.*, 2021, **57**, 392–400.

20 J. Lang, Y. Jin, X. Luo, Z. Liu, J. Song, Y. Long, L. Qi, M. Fang, Z. Li and H. Wu, *J. Mater. Chem. A*, 2017, **5**, 19168–19174.

21 Y. Fan, C. Deng, Y. Gao, Y. Ding, Y. Wu, S. Mo, Y. Yao, B. Liang, S. Lu, W. Qi and T. Tao, *Carbon N. Y.*, 2021, **177**, 357–365.

22 Z. Y. Wang, Z. X. Lu, W. Guo, Q. Luo, Y. H. Yin, X. Bin Liu, Y. S. Li, B. Y. Xia and Z. P. Wu, *Adv. Mater.*, 2021, **33**, 1–9.

23 C. Wei, Y. Wang, Y. Zhang, L. Tan, Y. Qian, Y. Tao, S. Xiong and J. Feng, *Nano Res.*, 2021, **14**, 3576–3584.

24 S. Yu, Z. Wu, J. Holoubek, H. Liu, E. Hopkins, Y. Xiao, X. Xing, M. H. Lee and P. Liu, *Adv. Sci.*, 2022, **9**, 1–8.

25 Y. An, Y. Tian, Y. Zhang, C. Wei, L. Tan, C. Zhang, N. Cui, S. Xiong, J. Feng and Y. Qian, *ACS Nano*, 2020, **14**, 17574–17588.